International Journal of
Geo-Information

Article

UAV Low Altitude Photogrammetry for Power Line Inspection

Yong Zhang [1], Xiuxiao Yuan [1,2,*], Yi Fang [1] and Shiyu Chen [1]

[1] School of Remote Sensing and Information Engineering, Wuhan University, 129 Luoyu Road, Wuhan 430079, China; zyong@whu.edu.cn (Y.Z.); fangyi@whu.edu.cn (Y.F.); csy_hy@whu.edu.cn (S.C.)
[2] Collaborative Innovation Center of Geospatial Technology, Wuhan 430079, China
* Correspondence: yuanxx@whu.edu.cn; Tel.: +86-27-6877-1228

Academic Editor: Wolfgang Kainz
Received: 21 October 2016; Accepted: 5 January 2017; Published: 12 January 2017

Abstract: When the distance between an obstacle and a power line is less than the discharge distance, a discharge arc can be generated, resulting in the interruption of power supplies. Therefore, regular safety inspections are necessary to ensure the safe operation of power grids. Tall vegetation and buildings are the key factors threatening the safe operation of extra high voltage transmission lines within a power line corridor. Manual or laser intensity direction and ranging (LiDAR) based inspections are time consuming and expensive. To make safety inspections more efficient and flexible, a low-altitude unmanned aerial vehicle (UAV) remote-sensing platform, equipped with an optical digital camera, was used to inspect power line corridors. We propose a semi-patch matching algorithm based on epipolar constraints, using both the correlation coefficient (CC) and the shape of its curve to extract three dimensional (3D) point clouds for a power line corridor. We use a stereo image pair from inter-strip to improve power line measurement accuracy by transforming the power line direction to an approximately perpendicular to epipolar line. The distance between the power lines and the 3D point cloud is taken as a criterion for locating obstacles within the power line corridor automatically. Experimental results show that our proposed method is a reliable, cost effective, and applicable way for practical power line inspection and can locate obstacles within the power line corridor with accuracy better than ±0.5 m.

Keywords: UAV remote sensing; power line inspection; dense matching; automatic detection of obstacles in power line corridor

1. Introduction

The expansion of the 500 kV extra high voltage (EHV) transmission line system for inter-provincial and large-span area power-supply tasks is presently a major project underway in China. Ensuring the safe operation of these lines is one of the important tasks for the power maintenance department at all levels. Buildings and tall plants, such as eucalyptus and bamboo, are typical obstacles threatening the safe operation of EHV transmission lines within power line corridors. Thus, power maintenance companies must devote a great deal of labor and material resources to power line corridor inspection, striving for the timely elimination of these safety risks.

Existing methods for power line inspection fall into three categories; manual, airborne LiDAR, and UAV inspection approaches. In manual ground-based inspection, each section in a segment of a power line corridor is assigned to a fixed inspection team. Manual visual interpretation is used to find and record obstacles along the power line corridor. It is difficult to conduct manual ground inspection for the erection of EHV transmission lines because EHV transmission lines are mainly located in areas that lack transportation. Obstacle interpretation depends on the conscientiousness and experience of inspection personnel, making inspection subjective. Moreover, manual inspection is dependent on visibility, so blind spots are unavoidable [1]. In airborne LiDAR power line inspection, a laser scanner is put onto a manned helicopter to obtain 3D point clouds of the objects and power line within the power line corridor. During post processing, the point cloud data is classified to extract objects and power lines within the line corridor. The distance between objects and power lines is used to locate obstacles. Existing research shows that although airborne LiDAR point clouds yield more accurate and less subjective inspection results than manual inspection [2], expensive airborne LiDAR systems have high maintenance costs [3] in practical operation. This seriously restricts the application and popularization of this method. For UAV power line inspection in China, the regulations on the UAV payload, flight height, velocity, and flight range are very strict. UAV flights must fly within visual range. If UAV flight does not meet the regulations, a license must be acquired from authority, and this will cause inconvenience and delays for power line inspection. However, UAVs have the advantages of low cost and ease of operation so are an attractive and popular option for power line inspection [4–6], and both fixed wing UAVs and multi-rotor UAVs have been adopted. UAV systems are flexible; digital cameras as well as video cameras are carried as UAV sensors [7]. Paper [8] comprehensively analyzed how computer vision technology is used in the operation and maintenance of transmission lines.

Little attention has been paid to using low-altitude UAV images for the accurate determination of distance between power lines and ground objects and for the automatic detection of obstacles found in power line corridors. In this paper, we propose a method of UAV power line inspection, through the automated detection of obstacles using photogrammetric approaches, thus fully exploiting the potential of UAV power line inspection. To use UAV to detect the obstacles within the power line corridor, three key problems need to be solved; 3D reconstruction of the ground of the power line corridor, power line measurement, and automatic recognition of obstacles. For ground reconstruction of the power line corridor, dense image matching techniques can be adopted to extract dense point clouds of the power line corridor; currently the extraction of dense point clouds from images obtained by low-altitude UAV is a very active research area in fields of photogrammetry and computer vision [9–11]. In UAV power line inspection, image-matching algorithms must be adapted to ground conditions with dense vegetation. At the same time, algorithms must be capable of extracting tree canopies and buildings stably and reliably. When shooting images of a power line corridor, the flight direction of the UAV must be consistent with the direction of the electric power line. Thus, the direction of the power line will be approximately parallel to the direction of the image's epipolar line. In a stereo mapping environment, it is hard to mark a power line correctly, and it is difficult to control the measurement error. Zheng et al. [12] proposed a method for power line positioning under the constraint of vertical line, yet there still exist large measurement errors. As a target moves up and down along the vertical line, the measure cursor moves along the epipolar line on the left and right images, and thus causes a measurement error.

In this paper, semi patch matching based on epipolar constraints (SPMEC) was proposed to extract the dense point clouds for the 3D reconstruction of ground objects in a power line corridor. It adapts to ground conditions with dense vegetation and can successfully extract tree canopies and rooftops stably and reliably. A stereo image pair from inter-strip is adopted to improve the power line stereo measurement accuracy, which changes the direction of the power line from approximately parallel to approximately perpendicular to the epipolar line for greater accuracy in stereo measurements. Finally, a power line is used as a bus bar, and a buffer space analysis is carried out according to the safety distance set in specification code so obstacles can be detected automatically.

2. Automatic Detection of Obstacles in Power Line Corridors

All the objects in the power line corridor with a distance to the power line less than the safety distance are defined as obstacles. If the 3D surface reconstruction of a power line corridor is complete, the power line measured, and a safe distance threshold given, then obstacles can be automatically located. Low-altitude UAV images, obtained after global navigation satellite system (GNSS) supported aerial triangulation [13], are the objects to be processed. First, SPMEC was proposed to extract the dense point clouds within the corridor for 3D reconstruction of the ground objects, including canopies, buildings, and other ground attachments. Then, manual power line measurement was applied to extract power line in stereo image pairs composed of corresponding images from different strips. Finally, along the power line direction at a set interval, we calculate the distance between the power line and the surface point cloud to determine whether it is within the safe distance range. An obstacle is identified when ground points are located within a distance less than the prescribed safety distance threshold.

2.1. Semi Patch Matching Algorithm Based on Epipolar Constraints

In this paper, epipolar images are the processing unit and a coarse to fine image matching strategy was adopted. In our proposed method, under the initial parallax constraint, a large matching window searches a one-dimensional image along the epipolar line and is used to extract the coarse matching seed points. If a parallax is continuous within an object and the same object has a consistent texture in the image, then the coarse matching seed point is considered the center of the fine matching window. In the segmented image, based on the segmented object of the seed point, a patch matching constraint is constructed (the segmentation result of an object only occupies part of the area within the $w \times w$ pixels range around the seed point, so it is called a semi patch). Then, the initial parallax of the points to be matched within the semi patch is determined according to the geometric conditions of the semi patch. A one-dimensional search is conducted within a smaller search range. Finally, an outlier detection algorithm is applied to eliminate the mismatched points.

(1) Construction of Parallax Triangulation Network

Relative orientation is conducted using the automatically measured image tie points in the stereo image pairs, and epipolar image pairs are generated. Meanwhile, the tie points are projected to the epipolar image, obtaining the coordinate and parallax of the tie point p_i (x, y) $(i = 1, 2, ..., n)$ in the left epipolar image, represented by P_{ei} (x_{ei}, y_{ei}, d_{ei}). According to the generation algorithm of an irregular triangulation network [14], a triangulated irregular network (TIN) is constructed using n relative orientation points, and the corresponding pseudo colors are given to the triangle vertexes, according to the difference of the parallax value d_{ei}. A parallax TIN is shown in Figure 1.

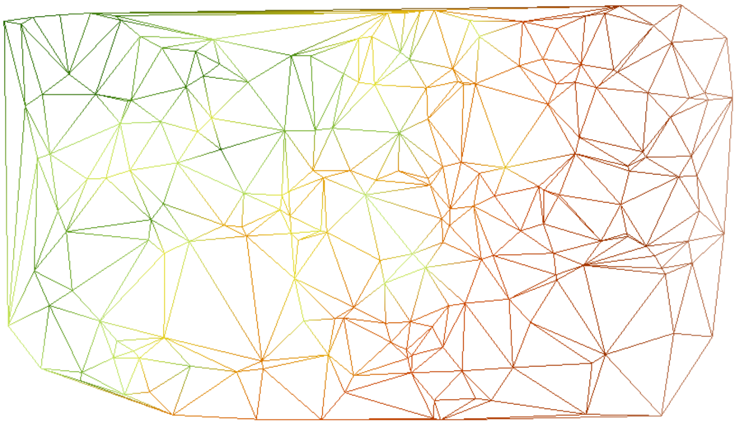

Figure 1. Initial Parallax Triangulation Irregular Network.

In Figure 1, triangle vertexes are composed of relative orientation points, and the corresponding pseudo colors are given to the triangle vertexes according to the difference of the parallax value.

(2) Stereo Image Matching Based on a Parallax Controlled Grid

First, a parallax controlled grid P_{egi} (x_{egi}, y_{egi}) is set to an interval of 15 pixels in the left epipolar image. Then, grid points are put into a parallax TIN, and the triangle $\Delta P_{ei}P_{ej}P_{ek}$ where P_{egi} lies is obtained. Bilinear interpolation is conducted on the parallaxes of the three vertices of the triangle [15] to obtain the initial parallax of P_{egi}. Then 61 × 61 pixels are used as the matching window. Slide within $[x_{egi} - 100, x_{egi} + 100]$ in the right epipolar image; for each pixel, the normalized correlation coefficient (CC) of the corresponding window is calculated according to Equation (1), and a CC curve is generated as shown in Figure 2.

$$\rho_{c,r} = \frac{\sum\limits_{i=0}^{n}\sum\limits_{j=0}^{n}[g_1(j,i)-\overline{g}_1]\times[g_2(j+c,i+r)-\overline{g}_2]}{\sqrt{\sum\limits_{i=0}^{n}\sum\limits_{j=0}^{n}[g_1(j,i)-\overline{g}_1]^2\times\sum\limits_{i=0}^{n}\sum\limits_{j=0}^{n}[g_2(j+c,i+r)-\overline{g}_2]^2}} \tag{1}$$

where (c, r) are the coordinates of the corresponding pixel of the center point pixel of the matching window in the right epipolar image, and the values $\overline{g}_1$ and $\overline{g}_2$ are the average gray levels of the corresponding matching window in the left and right epipolar image, respectively. The size of the matching window is n and i, j is the line number and column number of the pixels within the matching window, and $g_1(j,i)$ and $g_2(j,i)$ are the gray values of the pixel (j, i) in the left and right right epipolar image, respectively.

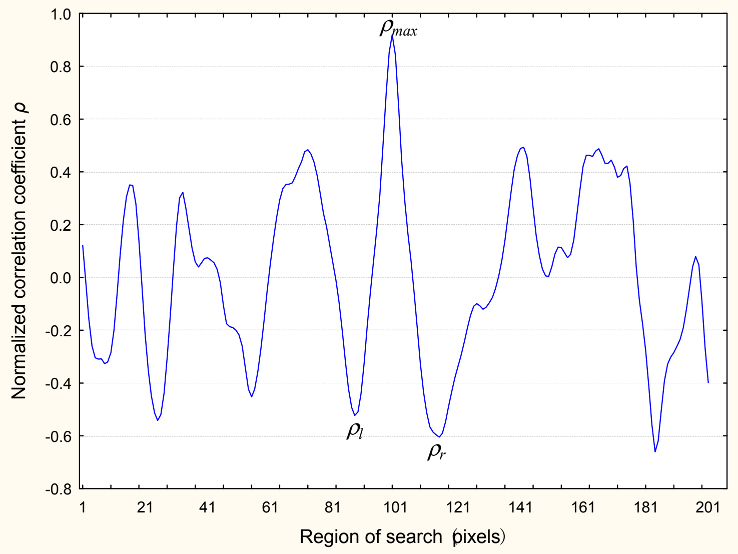

Figure 2. CC Curve.

In Figure 2, $\rho_{\max}$ is the peak value of the normalized CC of the matching window and searching window at the corresponding pixel. ρ_l and ρ_r are the normalized CC of the lowest points of the monotone decrease on both sides of the peak value respectively. To determine if the matching is successful we apply Equation (2) as follows:

$$\begin{cases} successful, & \text{when } \rho_{\max} \geq 0.9 \\ successful, & \text{when } \rho_{\max} < 0.9 \text{ and } |\rho_l - \rho_r| < 0.2 \text{ and } |l_l - l_r| < 5.0 \text{ and } [\rho_{\max} - (\rho_l + \rho_r)/2] \geq 0.6 \\ failed, & \text{else} \end{cases} \tag{2}$$

where l_l and l_r are the distances in pixels between the peak value and the lowest points on both sides of the peak value respectively.

It can be seen from Equation (2), in contrast to most matching algorithms based on a normalized CC, when designing similarity criterion, we use not only the value of the normalized CC but also the curve characteristics of the CC. During image correlation, when sliding the matching window, if the corresponding image point is found in the search region of the right image, then the CC will change following a law from small to large and then from large to small as the matching window gets closer and moves far away from the corresponding point. Isolated peaks are evident in the data; two sides of the peak value are approximately symmetrical (as shown in Figure 2). In Equation (2), $|\rho_l - \rho_r| < 0.2$ and $|l_l - l_r| < 5.0$ are used respectively to constrain the symmetry of both sides of the CC peak; $[\rho_{max} - (\rho_l + \rho_r)/2] \geq 0.6$ is used to constrain the distinctiveness of the CC peak.

As can be seen from Figure 3, matching window 1 has rich texture and the peak of the CC is greater than 0.9 within the search window, meaning a successful match; matching window 2 also has rich texture for it lies on the canopy, yet it is rather homogeneous. The CC peak is only 0.2; however, there is a symmetric shape in the CC curve near the peak and the CC difference between the peak and the trough is greater than 0.6. It is also a successful match. Matching window 3 lies in the shadow; the peak of the CC within the search window researches 0.6, but there is no obvious pattern of the CC curve shape, hence a failed match. From these three typical matching states, we can see that Equation (2) can improve successful matching rates without introducing too many mismatch points, compared to simply setting the threshold of the CC to a lower value in order to density match points.

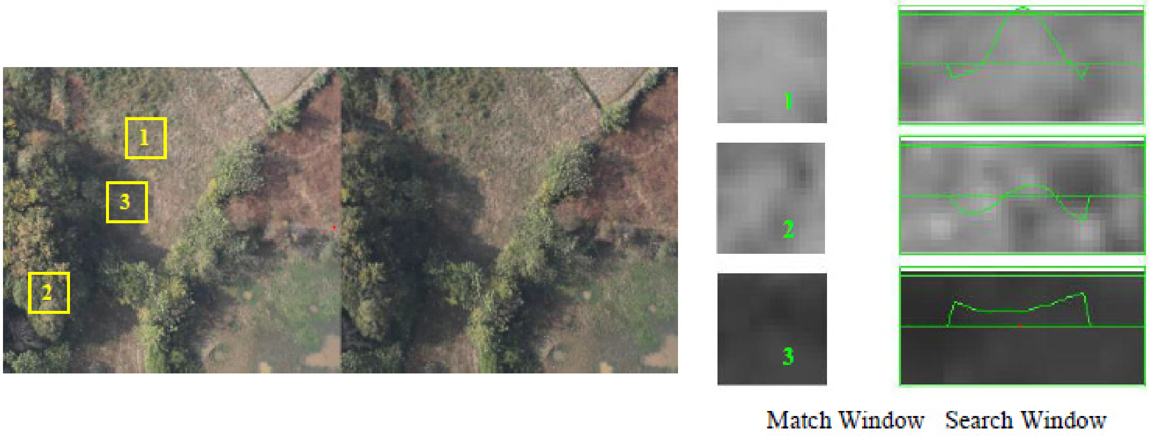

(a) (b)

Figure 3. Similarity judgment considering the shape of CC curve. (**a**) Matching window (**b**) Correlation coefficient curve.

(3) Semi Patch Dense Image Matching

We use Graph-Based image segmentation method [16] to segment the left epipolar image and the segmentation result is shown in Figure 4.

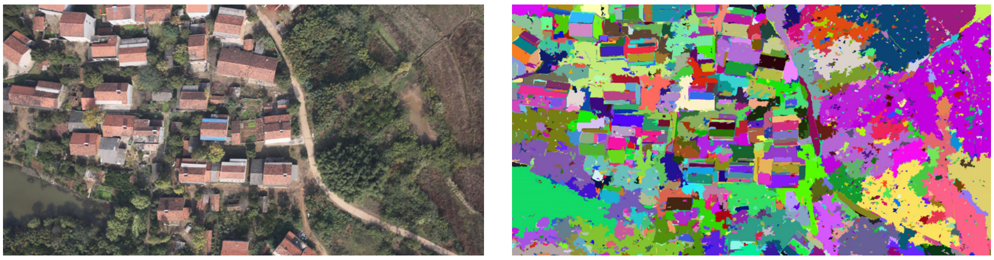

(**a**) (**b**)

Figure 4. Image Segmentation Result. (**a**) Original image (**b**) Segmented image.

For a pixel p_i to be matched, $P = \{p_1, p_2, ..., p_n\}$, the set of grid nodes located in the corresponding segmented area within the parallax regular gird network, and $D = \{d_1, d_2, ..., d_n\}$, the parallax of pixels in the set, can be obtained. Since the pixels in the same-segmented areas have similar texture features in a local neighborhood of objective space, assuming that the regular object surface has a consistent image texture, $\pi(p_x, p_y, d)$, the parallax space plane can be constructed using the image point coordinates within the set P and the corresponding parallax. Put p_i into π, the plane equation; then d_i, the initial parallax, can be obtained. Then taking 11 × 11 pixels as a matching window, slide within $[x_{egi} - 20, x_{egi} + 20]$ in the right epipolar image. For each pixel, the normalized CC of the corresponding window is calculated according to Equation (1). Then we determine if the matching was successful according to Equation (2). A comparation of the matched point cloud with and without using the semi patch is shown in Figure 5.

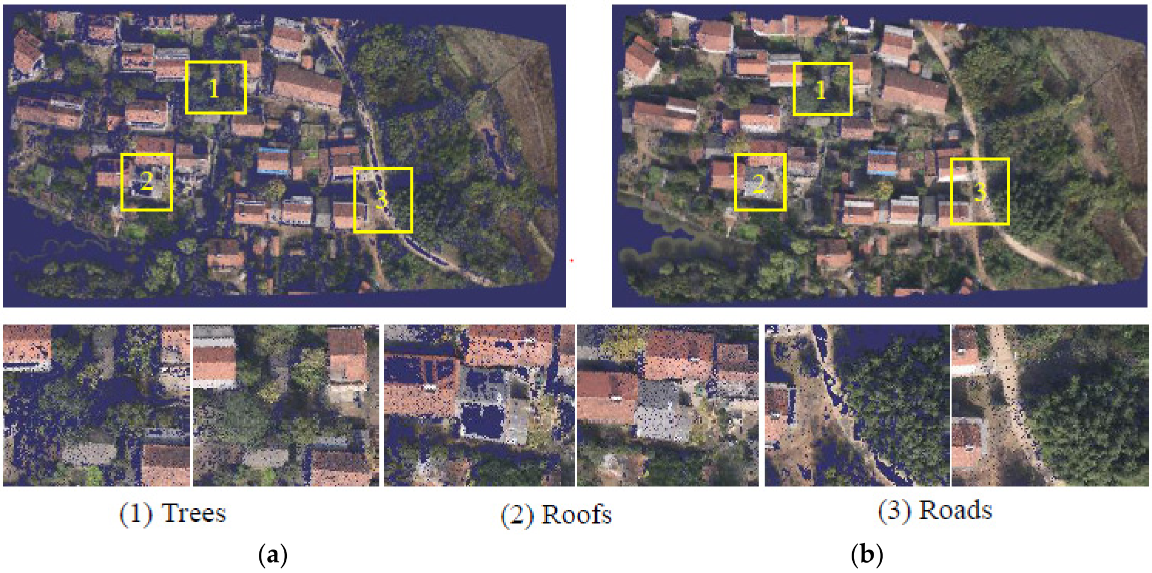

(1) Trees (2) Roofs (3) Roads

(a) (b)

Figure 5. Comparation of point cloud with/without using the semi patch dense match. (**a**) Match result without using semi patch (**b**) Match result using semi patch.

From Figure 5 we can see that the point cloud using the semi patch has fewer holes in the road and rooftop areas than that without using semi patch. Holes are caused by the homogenous texture in the match window and the initial parallax of the surounding objects. After using the semi patch, because the initial parallax of the match window is determined by the corresponding segment, the successful match rate improves, especially in roads and rooftop areas. The successful match rate in vegetation area improves as well.

(4) Eliminating Mismatched Points

There always exists some outlier points in the point cloud, causing false alarms in power line corridor inspection, which need to be eliminated. The distance between the outlier points and the rest points is different from the distance between non-outlier points and the rest points. For a point cloud containing N points, if the longest distance L among those non-outlier points and the probability of the outlier b are set, a non-outlier point count, M, can be estimated. Then we count a number NUM for each point PT in the point cloud. If NUM is less than M, an outlier is found. NUM is calculated as follows: for each point PT in the point cloud, the initial NUM is set to zero, then iterate through the point cloud. If the distance between current point and PT is less than L, add one to NUM.

Assume that the point to be matched is $p(x, y, z)$; the matching results T is expressed as the set of p. If the set has a total of n points, the distance between any two points in the set can be expressed as:

$$l(i,\ j) = \sqrt{(x_i - x_j)^2 + (y_i - y_j)^2 + (z_i - z_j)^2} \quad (p_i, p_j \in T) \tag{3}$$

Assume that the probability of mismatched points in the set of matched points is b, so the number of correctly matched points that may be included in the point set is $M = (1.0 - b) \times n$. For o, any point in T, if L, the distance, is given, N, the number of points within the range with o as the origin, L as the radius can be obtained. If $N < M$, o is an outlier; otherwise, it is a correctly matched point. Thus, the criterion used in this paper depends on the two parameters of b and L. Experiments have shown that it is more appropriate to take $b = 20\%$, and L is derived by using RANSAC [17] method. For the ith iteration, randomly sample a point from the point cloud, and calculate the standard deviation of the distance between this point and every point in the remaining point cloud. After removing those points whose distance is greater than three times of this standard deviation, take the biggest distance value as the L_i. We sample the point cloud for 500 time and $L = argmin\{L_i; i = 0, ..., 500\}$.

Following the 4 steps above, taking the epipolar images as objects to be matched, the image tie points obtained by GNSS-supported aerial triangulation were used as an initial condition; a triangular irregular network controlled by initial parallax was constructed. After parallax controlled grid interpolation, semi-patch matching, and mismatched points eliminating, ground dense point clouds can be obtained as shown in Figure 6. The texture color of the point clouds are taken from the left epipolar image.

Figure 6. Dense 3D Point Clouds Extracted by SPMEC (the three colorful lines represent three power lines).

As seen in Figure 6, the SPMEC achieves 3D ground reconstruction of the power line corridor, with morphologically intact canopies, regular building edges, and clear small building components such as chimneys and solar water heaters providing an accurate digital surface model for automated detection of the obstacles within power line corridors. For more information about SPMEC, please see Video S1 (Supplementary Materials). The video demonstrates the reconstruction of three typical landscapes within power line corridor using SPMEC: the first scene includes both the power line and ground surface, second scene is of a rural settlement and the third scene is of a mountainous area.

2.2. Power Line Measurement Based on Stereo Image Pair from Inter-Strips

There are two flight strip images taken by UAV during power line corridor inspection; each side of the power line has one strip. The epipolar line direction of the stereo images pair within a strip is almost parallel to the power line, making it difficult for measure cursor to be placed on the corresponding points on the power line, and the power line measurement may fail.

As shown in Figure 7, there are two flight strips along power line. Pyramids stand for the position and orientation of the images. Pseudo color points are the pass points. During manual stereo observation, the height of the measurement cursor is adjusted by the x-parallax. Because the direction of the power line is approximately parallel to the epipolar line, when adjusting the x-parallax, the movement track of the measurement cursor coincides with the epipolar line (shown in Figure 8a), making it hard to measure the corresponding point on the power line. To make it easy for stereo measure, we should make the epipolar line of the stereo image pair perpendicular to the power line, such stereo image pairs can be acquired by using the images on different sides of the power line.

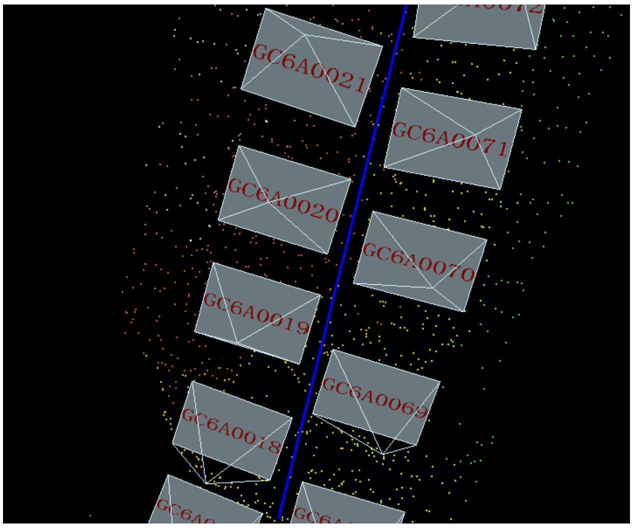

Figure 7. Image position on both sides along the power line.

(**a**)

(**b**)

Figure 8. Stereo image pair for power line measurement. (**a**) Stereo image pair form inter-strips (**b**) Stereo image pair form inter-strips.

As seen in Figure 8b, by using stereo image pairs that form inter-strips for power line measurement, the base line direction of the stereo image pair is approximately perpendicular to the direction of the power line. Therefore, the epipolar direction of the stereo image pairs is approximately perpendicular to the direction of the power line; the intersection point of the epipolar line and the power line is the corresponding point on the power line.

When performing manual measurement, the operator only needs to adjust the measure cursor (red cross) at the corresponding point on the power line. Due to gravity, the power line should to be modeled using a polyline instead of a single straight line. Thus, the whole power line between two posts needs to measure about 30 pairs of corresponding points to model the polyline. The accuracy of a manual measurement of the power line only depends on the ground resolution of UAV images. In order to acquire sufficient image resolution, we designed a suitable flight height using the focal length of the camera before power line corridor inspection. Hence, for power line measurement, the only thing required is to make sure that the left and right measuring cursor align at the corresponding power line.

2.3. Automatic Detection of Obstacles in Power Line Corridor

After extracting the power line and 3D point clouds of the power line corridor, we take the power line as the bus line and construct a spatial buffer zone around power line with a safe distance of r (shown in Figure 9). An obstacle can be detected when the 3D point clouds intersect with the spatial buffer zone.

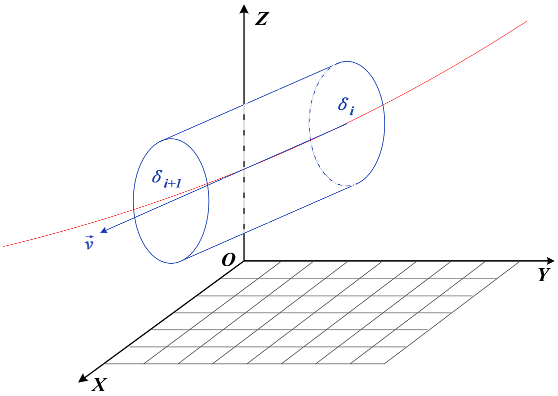

Figure 9. Diagram of Principle for Automatic Obstacle Detection.

In Figure 9, the power line is divided into n segments with δ as step distance. The terminals can be expressed as $\delta_1, \delta_2, ..., \delta_n, \delta_{n+1}$. When δ is small enough, each segment can be regarded as a straight line. The direction vector of the line segment constituted by $\delta_i(X_i, Y_i, Z_i)$ and $\delta_{i+1}(X_{i+1}, Y_{i+1}, Z_{i+1})$ is $\vec{v} = \begin{bmatrix} A & B & C \end{bmatrix}^T = \begin{bmatrix} X_{i+1} - X_i & Y_{i+1} - Y_i & Z_{i+1} - Z_i \end{bmatrix}$. If there exist points in digital surface point clouds that satisfying the following condition:

$$\begin{cases} (At - X + X_i)^2 + (Bt - Y + Y_i)^2 + (Ct - Z + Z_i)^2 \leq r^2 \\ \frac{|AX+BY+CZ-(AX_i+BY_i+CZ_i)|+|AX+BY+CZ-(AX_{i+1}+BY_{i+1}+CZ_{i+1})|}{\sqrt{A^2+B^2+C^2}} \leq \delta \end{cases} \tag{4}$$

then these points are considered as obstacles. The distance between these points and the straight line is the distance between the obstacles and the power line. In this way, the exact position of the detected obstacles is determined.

3. Results and Discussion

3.1. Experiments and Analysis of the Obstacles Detection of Power Line Corridor

In order to verify the validity of the proposed method, the authors wrote an experimental program using the VC++ language. A section of a 220 kV power line in Yichang, Hubei Province, China, about 16.5 km in length, was selected for an inspection experiment, which is a typically difficult area for power line corridor inspection. A fixed wing UAV (shown in Figure 10) with a Nikon D810 camera (focal length 50 mm, CMOS Sensor, 35.9 mm × 24.0 mm, 7360 × 4912 pixels, pixel size 4.88 µm) was adopted for low-altitude photography of the power line corridor; images were shot from a fix distanced. The strip overlap and the side-strip overlap were both 80%. The UAV was equipped with a GNSS receiver (GPS L1/L2). The exposure point coordinates are obtained using precise point position (PPP). The coordinates were applied in the GNSS-supported aerial triangulation.

The ground sample distance (GSD) was about 3.5 cm; two sorties were flown and 1066 images obtained. The images are clear, and the contrast is moderate, which can meet the requirements for power line inspection. The exterior orientation parameters of the images were obtained by GNSS-Supported aerial triangulation; we split the long strip into segments in every 10 km, in order to control the bad effect caused by long strip in bundle adjustment, and all the images were processed according to the procedures mentioned in Section 2. Ground 3D point clouds extracted from stereo image pairs along each strip and some segments of power line using inter-strip image pairs are shown in Figure 11.

In Figure 11, the ground 3D point clouds were extracted by SPMEC, the red points are obstacles, and the red, yellow, and blue wires are obtained by stereo image pair from inter-strip and manual measurement. The towers are existing 3D models put in the scene to make it more intuitive.

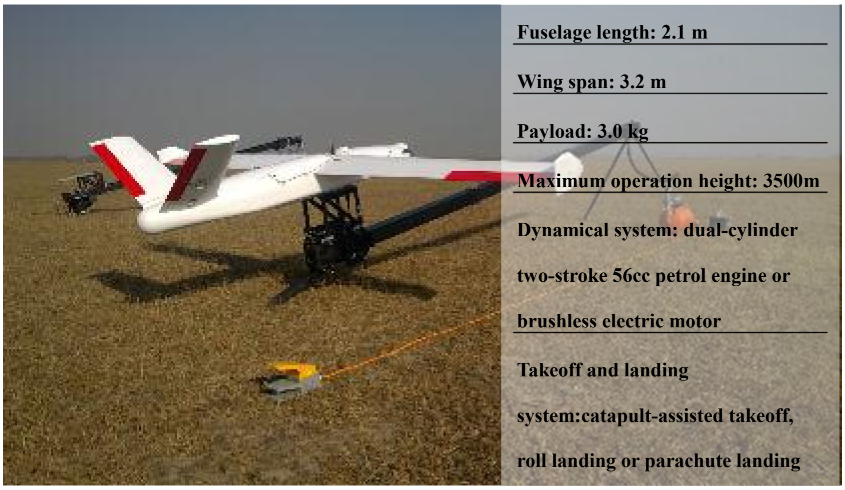

Figure 10. Diagram of fixed wing UAV.

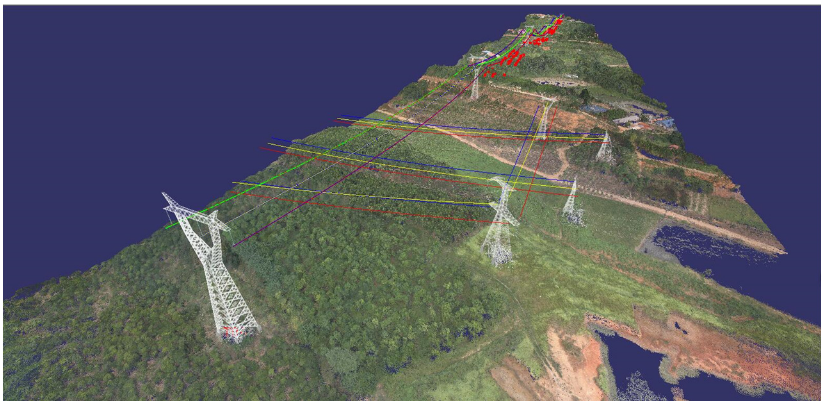

Figure 11. Diagram of Ground 3D Point Clouds and Power Lines within the Power Line Corridor.

3.2. Detection of Obstacles in the Power Line Corridor

Based on the results shown in Figure 11, when the safety distance threshold between the power line and 3D point clouds was set to 15 m, the locations of obstacles were listed in Table 1 using the method mentioned in Section 2.3; one obstacle is shown in Figure 12.

Table 1. Distribution of Some Obstacles within the Power Line Corridor (safety distance threshold is 15 m).

Tower Section	Position of the Obstacle (m)	Distance between the Obstacle and the Power Line (m)
K182~K183	133.0–135.0	14.658
	180.5–185.0	13.990
	188.5–189.0	14.865
	201.5–268.0	11.182
	119.5–123.5	12.137
	191.5–201.5	12.518
	204.0–206.0	13.809

As shown in Table 1, the first column lists number of the towers, the second column represents the distance between the obstacles and K182 tower, and the third column shows the distance between the obstacles and power lines.

As shown in Figure 12, an obstacle has a certain continuity in space. Therefore, in Table 1, the position of the obstacle is expressed as a continuous range. The minimum distance within this range is taken as the distance between an obstacle and the power line. The measurement accuracy of the obstacles will be further verified.

Figure 12. Diagram of an obstacle within the Power Line Corridor.

Since the power line selected for experiment is operational, it is impossible to measure the distance of the power line and the objects directly. It is also difficult to aim at the power line with a total station instrument. Consequently, in this paper, two methods are used to check the accuracy of power line inspection and the measurement of ground point clouds. A field investigation was conducted and the results were reviewed by manual inspection to confirm the validity of the method and the accuracy of the automatic detection.

Method 1: A Trimble TX8 ground laser scanner was used for 3D scanning of the tower K182 and its power line. Firstly, the GPS Real-time kinematic (RTK), Trimble R10, was used for accurately locating the position of the TX8 scanner, and, then, the orientation point coordinates of the TX8 were measured and equipment orientation was completed. The 3D laser point cloud was obtained by 3D scanning of the TX8 as shown in Figure 13. We overlaid the point cloud data collected by the TX8 scanner and the power line vectors measured by manual work. Taking the power line captured by the TX8 as the 'ground trues', we set a section with an interval of 1 m; every section has a gravity center of the point cloud and an intersection point of the power line. We calculated the elevation difference between the gravity center and the intersection point. Then, the error in the elevation difference was taken as criterion to evaluate the measurement precision of the power line. Several sampling points and the elevation differences are listed as shown in Table 2.

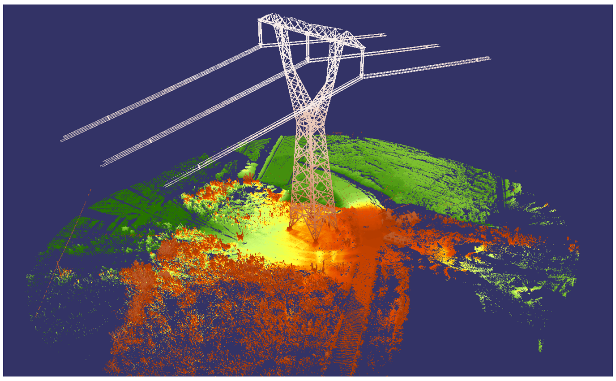

Figure 13. Diagram of Point Cloud Scanned by Laser 3D Scanner at K182.

It can be seen from Table 2 that the power line measurement based on manual work adopted in this paper transforms the direction of the power line from being approximately parallel to the epipolar direction to being approximately perpendicular to the epipolar direction, so that the measuring cursor is accurately aligned with the power line while moving along the epipolar line. Manual measurement accuracy of the elevation reached ±0.326 m on the ground.

Table 2. Distribution of Elevation Difference of Sampling Points in the Power Line Profile (Unit: m).

Elevation of 3D Point Cloud Gravity Center	Elevation of Manual Measurement	Elevation Difference
138.313	138.720	0.407
135.709	135.644	−0.065
133.423	133.632	0.210
131.511	131.414	−0.097
129.975	130.411	0.436
128.813	128.804	−0.009
128.027	128.164	0.137
128.632	128.053	−0.579
129.721	129.765	0.044
131.185	130.857	−0.328
133.024	133.308	0.284
135.237	135.683	0.446
137.826	137.376	−0.450
140.790	141.163	0.373
Root Mean Square Error of the Elevation Difference: 0.326		

Method 2: 20 distinct ground objects were selected within the power line corridor, whose 3D ground coordinates were measured in the field by GPS RTK. The accuracy of planimetry and elevation both reached the centimeter level in the ground [18], so were regarded as 'ground trues'. The 3D coordinates obtained in the stereo measuring environment were compared with these true values one by one to evaluate the accuracy of the automatically extracted dense 3D point cloud. Differences between the coordinates of all the checking points are listed in Table 3.

Table 3. Difference of Coordinates of the Checking Points (Unit: m).

Checking Point	*X*	*Y*	Planimetry	Elevation
1	0.020	−0.034	0.040	0.383
2	0.043	−0.014	0.045	0.126
3	0.043	0.007	0.044	0.103
4	−0.090	−0.015	0.091	0.278
5	−0.011	−0.076	0.077	0.156
6	−0.017	0.036	0.039	−0.182
7	−0.129	−0.088	0.156	0.408
8	0.084	−0.003	0.084	−0.133
9	−0.006	−0.001	0.006	0.005
10	0.053	0.081	0.097	0.421
11	0.013	−0.180	0.180	0.177
12	0.017	−0.024	0.029	0.162
13	−0.005	−0.099	0.100	0.276
14	0.013	0.124	0.125	−0.578
15	−0.119	−0.006	0.119	0.269
16	−0.045	0.082	0.094	−0.391
17	−0.040	0.020	0.045	−0.234
18	−0.053	−0.059	0.079	0.356
19	0.086	−0.014	0.087	−0.196
20	−0.181	0.129	0.222	−0.442
Maximum Difference	−0.181	−0.180	0.222	−0.578
Root Mean Square Error	0.071	0.075	0.103	0.302

It can be seen from Table 3 that the coordinates of distinct objects obtained by manual observation in the stereo measuring environment are quite consistent with the coordinates measured in the field. The maximum differences of the planimetry and elevation of the point cloud are 0.222 m and −0.578 m, and the root mean square errors are ±0.103 m and ±0.302 m, respectively. Further analysis shows that if the measurement error of 'ground trues' was deducted, the elevation measurement accuracy obtained by the two methods is basically the same. Consequently, the results in Table 3 can be regarded as evidence in evaluating the accuracy of our method for extracting power line and ground point clouds.

In addition, the dense image matching process is similar to that of manual stereo measures. Using image matching to replace the manual stereo measure and using parabolic fitting during image matching to further increase the matching accuracy, an accuracy of ±0.29 pixels can be achieved [19], which significantly decreases the manual measurement error. Hence, compared with the manual stereo measure, dense image matching has a higher accuracy.

It can be seen from Tables 2 and 3 that the elevation accuracies of power line and the ground 3D point clouds were ±0.326 m and ±0.302 m, respectively. Based on error propagation principles, the relative elevation difference accuracy of power line and ground 3D point clouds was estimated at ±0.444 m. Our proposed method achieved distance-measuring accuracy better than ±0.5 m; such accuracy meets the requirements of power line inspection.

4. Conclusions

In this paper, a low-altitude UAV based power line inspection method for obstacles in power line corridors was proposed. The images processed by the GNSS-supported aerial triangulation were the input, and the obstacle distribution report was the output. We focused on solving three problems; 3D reconstruction of the ground surface of the power line corridor, measurement of the power line, and automatic recognition of obstacles. According to the similarity measurement, which takes the normalized CC and the shape of the coefficient curve into consideration, dense point clouds of canopies and buildings with regular outlined can be extracted by SPMEC in rural areas with lush vegetation. Even small building components such as the chimneys and solar water heaters can be clearly expressed.

A stereo image pair from inter-strips was used to build a measurable stereo image pairs, transforming the power line from being approximately parallel to the direction to being approximately perpendicular to it, which has effectively improved the measurement accuracy of the power lines. Experimental results show that our proposed approach can automatically find and accurately locate the obstacles in the power line corridors with measurement accuracies better than ±0.5 m, providing a new means for quantitative inspection of obstacles to the safe operation of ultra-high voltage transmission lines. However, there are still some issues that need to be addressed in order to improve the automation of power line inspection, especially the measurement of automatic power lines. The bottleneck of the automation is power line extraction from images, which is still a challenging task and will be further studied.

Supplementary Materials: The following are available online at www.mdpi.com/2220-9964/6/1/14/s1. Video S1: Power line inspection demo. This video demonstrates the reconstruction of three typical landscapes within power line corridor using SPMEC: the first scene includes both the power line and ground surface, second scene is of a rural settlement and the third scene is of a mountainous area.

Acknowledgments: This work has been supported by the National Natural Science Foundation of China (Grant No. 41371432).

Author Contributions: Yong Zhang developed the algorithm and conducted the primary data analysis, as well as crafting the manuscript. Xiuxiao Yuan advised on and contributed to the data analysis, as well as providing remote sensing experience and significantly editing the manuscript. Yi Fang and Shiyu Chen carried out the experiments and advised on research question generation and the reshaping of the manuscript.

Conflicts of Interest: The authors declare no conflict of interest.

References

1. Mu, C. Research on Extraction Method of Power Line Corridor Feature Based on Multi Remote Sensing Data. Ph.D. Dissertation, Wuhan University, Wuhan, China, 2010.
2. Kuhnert, K.D.; Kuhnert, L. Light-weight sensor package for precision 3D measurement with micro UAVs E.G. power-line monitoring. *Int. Arch. Photogramm. Remote Sens. Spat. Inf. Sci.* **2013**, *XL-1/W2*, 235–240. [CrossRef]
3. Ahmad, J.; Malik, A.S.; Xia, L.; Ashikin, N. Vegetation encroachment monitoring for transmission lines right-of-ways: A survey. *Electr. Power Syst. Res.* **2013**, *95*, 339–352. [CrossRef]
4. Chang, A.; Wang, C. Mission planning of the flying robot for powerline inspection. *Prog. Nat. Sci.* **2009**, *19*, 1357–1363.
5. Mulero-Pázmány, M.; Negro, J.J.; Ferrer, M. A low cost way for assessing bird risk hazards in power lines: Fixed-wing small unmanned aircraft systems. *J. Unmanned Veh. Syst.* **2014**, *2*, 5–15. [CrossRef]
6. Cerón, A.; Mondragón, I.F.; Prieto, F. Visual based navigation for power line inspection by using virtual environments. *Proc. SPIE* **2015**, *9406*, 94060J:1–94060J:7.
7. González-Jorge, H.; Puente, I.; Roca, D.; Martínez-Sánchez, J.; Conde, B.; Arias, P. UAV potogrammetry monitoring application to the monitoring of rubble mound breakwaters. *J. Perform. Constr. Facil.* **2016**, *30*, 04014194. [CrossRef]
8. Miralles, F.; Pouliot, N.; Montambault, S. State-of-the-art review of computer vision for the management of power transmission lines. In Proceedings of the IEEE International Conference on Applied Robotics for the Power Industry (CARPI), Foz do Iguassu, Brazil, 14–16 October 2014.
9. Hirschmüller, H. Accurate and efficient stereo processing by semi-global matching and mutual information. In Proceedings of the IEEE Computer Society Conference on CVPR, San Diego, CA, USA, 20–25 June 2005.
10. Yasutaka, F.; Jean, P. Accurate, dense, and robust multiview stereopsis. *IEEE Trans. Pattern Anal. Mach. Intell.* **2010**, *32*, 1362–1376.
11. Bleyer, M.; Rhemann, C.; Rother, C. Patchmatch stereo—Stereo matching with slanted support windows. In Proceedings of the British Machine Vision Conference, Dundee, UK, 29 August–2 September 2011.
12. Zheng, S.; Hu, H.; Huang, R.; Ji, Z. Realtime ranging of power transmission line. *Geomat. Inf. Sci. Wuhan Univ.* **2011**, *36*, 704–707.
13. Yuan, X.X. A novel method of systematic error compensation for a position and orientation system. *Prog. Nat. Sci.* **2008**, *18*, 953–963. [CrossRef]

14. Shewchuk, J.R. Delaunay refinement algorithms for triangular mesh generation. *Comput. Geom.* **2002**, *22*, 21–74. [CrossRef]
15. Gribbon, K.T.; Bailey, D.G. A novel approach to real-time bilinear interpolation. In Proceedings of the Delta IEEE International Workshop on Electronic Design, Test and Applications, Perth, Australia, 28–30 January 2004; pp. 126–131.
16. Felzenszwalb, P.F.; Huttenlocher, D.P. Efficient graph-based image segmentation. *Int. J. Comput. Vis.* **2004**, *2*, 167–181. [CrossRef]
17. Fischler, M.A.; Bolles, R.C. Random Sample Consensus: A paradigm for model fitting with application to image analysis and automated cartography. *Commun. ACM* **1981**, *24*, 381–395. [CrossRef]
18. Lemmon, T.R.; Gerdan, G.P. The influence of the number of satellites on the accuracy of RTK GPS positions. *Aust. Surviv.* **1999**, *44*, 64–70. [CrossRef]
19. Zhang, Z.X.; Zhang, J.Q. *Digital Photogrammetry*; Wuhan University Press: Wuhan, China, 1997.